Computational analysis of M–O covalency in M(OC6 H5)4(M = Ti, Zr, Hf, Ce, Th, U)

Journal Name

ARTICLE

Computational analysis of M-O covalency in $M(OC_6H_5)_4$ (M = Ti, Zr, Hf, Ce, Th, U)

Received 00th January 20xx,
Accepted 00th January 20xx

DOI: 10.1039/x0xx00000x

www.rsc.org/

Victoria E. J. Berryman,*[a] Zoë J. Whalley,[a] Jacob J. Shephard,[b] Tatsumi Ochiai,[b] Amy N. Price,[b] Polly L. Arnold,[b] Simon Parsons[b] and Nikolas Kaltsoyannis*[a]

A series of compounds $M(OC_6H_5)_4$ (M = Ti, Zr, Hf, Ce, Th, U) is studied with hybrid density functional theory, to assess M-O bond covalency. The series allows for the comparison of d and f element compounds that are structurally similar. Two well-estabilished analysis methods are employed: Natural Bond Orbital and the Quantum Theory of Atoms in Molecules. A consistent pattern emerges; the U-O bond is the most covalent, followed by Ce-O and Th-O, with those involving the heavier transition metals the least so. The covalency of the Ti-O bond differs relative to Ce-O and Th-O, with the orbital-based method showing greater relative covalency for Ti than the electron density-based methods. The deformation energy of *r*(M-O) correlates with the d orbital contribution from the metal to the M-O bond, while no such correlation is found for the f orbital component. f orbital involvement in M-O bonding is an important component of covalency, facilitating orbital overlap and allowing for greater expansion of the electrons, thus lowering their kinetic energy.

Introduction

The extent to which the 5f orbitals participate in the bonding in actinide systems is a rich area of research. A demand for increased understanding of bonding in this region of the periodic table is growing, as pressure mounts for advances in technologies for reprocessing and disposal of nuclear waste. Although much progress has been made there is still debate about the appropriate tools to describe covalency and bonding in molecular f element compounds. Furthermore, there is a lack of understanding of periodic trends in bonding within the lanthanide and actinide series and how they change with oxidation state and ligand environment.[1–4]

The mixing of metal and ligand orbitals is proportional to the spatial overlap between them and inversely proportional to the difference in their energies.[5–9] Strong mixings can therefore arise when there are small energy differences between metal and ligand orbitals (*e.g.* in compounds of the so-called minor actinides, americium and curium) but only orbital overlap results in electronic charge accumulation in the internuclear region. Equating covalency with orbital mixing, we therefore have two sources of covalency; orbital overlap driven and orbital energy driven. Computational tools must consider both mechanisms to fully explore the nuanced property of covalency and thus, both an orbital-based approach and an electron topological approach are employed in this study. For the former, localized bonding orbitals are analysed with the Natural Bond Orbital (NBO) method[10] and for the latter, the quantum theory of atoms in molecules (QTAIM)[11] is employed. The NBO method moves beyond the, often delocalised, canonical molecular orbitals to optimally express a set of molecular orbitals with Lewis-like bonding. The QTAIM approach uses the electron density to partition the molecule into atomic regions for which atomic properties can be defined, while providing a measure of electron density involved in the bonding interactions between them.

We recently reported a diuranium(III) compound which exhibits interesting behaviour at high pressure.[12] Agostic interactions between the U and C–H groups of the $N(SiMe_3)_2$ ligands emerge only at high pressure (3.2 GPa), as evidenced by NBO and QTAIM analyses. While this was the first high pressure study of an organoactinide complex, pressure has proven to be a useful tool to study other actinide materials, in particular, for understanding the behaviour of the 5f orbitals of uranium and plutonium.[13,14] Our results stimulated us to further explore weak interactions, and covalency, at high pressure. In this paper we establish a computational approach to analyse and interpret the effects of shortening a metal-ligand bond, such as may occur at high pressure. We are currently studying the effects of pressure on An(IV) tetra(aryloxide) complexes experimentally. The targets chosen here ($M(OC_6H_5)_4$ (M = Ti, Zr, Hf, Ce, Th, U)) are models for these experimental systems; we seek to establish the methodology and computational tools which will be used in future analysis of these, and other, experimentally-characterised systems.

Methods

[a] Dr. V. E. J. Berryman, Z. Whalley, Prof. N. Kaltsoyannis, School of Chemistry, The University of Manchester, Manchester, M13 9PL (UK)
[b] Dr. Jacob J. Shephard, Dr. Tatsumi Ochiai, Dr. Amy Price, Prof. P. L. Arnold, Prof. S. Parsons, EaStCHEM School of Chemistry, University of Edinburgh The King's Buildings, Edinburgh, EH9 3FJ (UK).
Electronic Supplementary Information (ESI) available: [details of any supplementary information available should be included here]. See DOI: 10.1039/x0xx00000x

Density functional theory (DFT) was employed throughout this study within the Gaussian 09 software package.[15] The hybrid density functional approximation, PBE0,[16,17] was used with Grimme's D3[18] and the Becke-Johnson damping parameters[19–22] for dispersion corrections and was selected based on previous benchmarking studies of an analogous organoactinide complex. These data are presented in Table SI1 of the Supplementary Information. Ahlrichs' polarized triple-ζ basis sets were employed for Ti and non-metal atoms (H, C and O).[23,24] All other metal atoms were treated with Stuttgart-Bonn small-core relativistic effective core potentials (ECP), replacing 28 electrons in Ce and Zr, and 60 electrons in Hf, Th and U, in combination with the associated segmented valence basis sets.[25–29] The ultrafine grid option was used for numerical integration; other parameters were set to their default values. The harmonic vibrational frequencies were used to verify the optimized geometries as true energetic minima.

The Ti system was also computed using a relativistic ECP, to replace the 10 core electrons; however, the NBO analysis could not be successfully executed in this case. That said, differences in other data computed with the ECP and the all electron basis sets were minimal. For example, optimized *r*(Ti-O) distances differed by less than 0.006 Å and the relative energies for the shortening of *r*(Ti-O) differed by a maximum of 2 kJ·mol^{-1}. QTAIM metrics also showed negligible differences (*e.g.* ρ_{BCP} values were within 0.002 au, and δ(M,O) and -(G_{BCP}/V_{BCP}) values were within 0.006) and both basis set schemes yielded the same trends in QTAIM metrics relative to the other systems.

Metal-ligand bonding orbitals were analysed via the Natural Localized Molecular Orbitals computed with the NBO software package.[10] The CHOOSE option was employed in NBO to impart a consistent bonding scheme in all systems which allowed for comparison of analogous overlap integrals in M-O bonding. Electron density-based analysis of metal-ligand bonding utilized the QTAIM[11] implemented in the AIMAll software package.[30]

Results and discussion

All of our target systems adopt C_2 symmetry, and key structural parameters are shown in Table 1. The Ti-O-C angle is fixed to the average of the Zr and Hf systems because the optimized ∠(Ti-O-C) of 141° differed significantly from the other systems, and we wish to ensure consistency across the geometries studied. This fixing produces a modest energy difference of 7 kJ·mol^{-1} vs fully optimised $Ti(OC_6H_5)_4$, and negligible changes to the metrics studied herein. To probe the changes in chemical bonding over a range of M-O bond distances, $M(OC_6H_5)_4$ were optimized and subsequently *r*(M-O) was shortened in 0.02 Å increments to –0.12 Å from the optimized values. A shortening of the *r*(M-O) bond by –0.12 Å represents a 6.7 % change for the Ti system (the shortest M–O bond) and a 5.6 % change for the Th system (the longest M–O bond). In these calculations, the *r*(M-O) parameter is fixed and all other parameters are optimized. Upon shortening of *r*(M-O), modest increases in the M-O-C angle occur, between 1° and 8°, while no other significant structural changes are observed. Energetic data from these scans are shown in Figure 1, with a trend of Ti>Hf>Zr>Th≈U>Ce. There is clear separation between the d block and f block elements, such that deformation energy for *r*(M-O) is greatest for the transition metals, followed by the actinides, and finally the lanthanide system, $Ce(OC_6H_5)_4$.

Table 1: Optimized structural parameters for $M(OC_6H_5)_4$. Average values reported. ∠(O-M-O) is the angle between the closest ligand pairs.

Compound	*r*(M-O), Å	∠(M-O-C), °	∠(O-M-O), °
$Ti(OC_6H_5)_4$	1.785	171.0†	108.8
$Zr(OC_6H_5)_4$	1.937	172.0	109.7
$Hf(OC_6H_5)_4$	1.919	170.1	109.5
$Ce(OC_6H_5)_4$	2.086	172.4	105.2
$Th(OC_6H_5)_4$	2.147	177.4	107.9
$U(OC_6H_5)_4$	2.088	172.5	102.4

†Ti-O-C angle fixed.

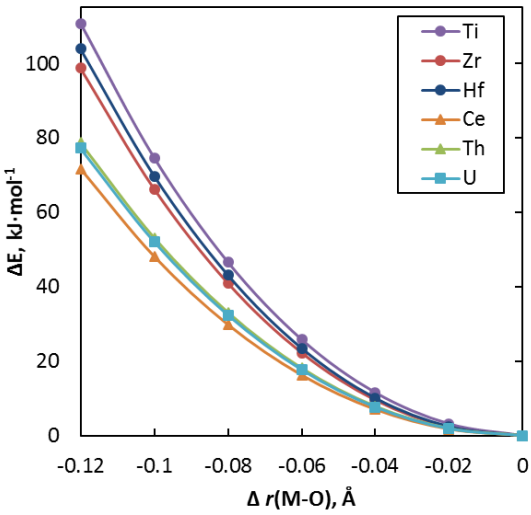

Figure 1: Relative energy changes as a function of *r*(M-O) in $M(OC_6H_5)_4$.

Natural localized molecular orbital analysis

The natural localized molecular orbitals (NLMOs) enforce maximum occupancy character, limited to integer occupancy. They are a complete and orthonormal set, able to describe exactly any property of the wave function, ψ. They have the advantage of typically being much more localised than the canonical orbitals, representing a Lewis-like structure and thus providing a conceptually intuitive picture of chemical bonding. Each orbital can be uniquely associated with a corresponding pre-orthogonal set of hybrid orbitals (PNHO). These PNHOs remain orthogonal to the atomic orbitals but have non-vanishing overlap integrals with PNHOs on other atoms, allowing for the overlap of these PNHOs to be assessed.

Each M-O interaction in our systems can be defined by three NLMOs, one σ-type and two π-type bonding orbitals. Representations of these three NLMOs are shown in Figure 2 for $Ti(OC_6H_5)_4$ and $U(OC_6H_5)_4$ and are typical of the d block and f block

systems, respectively. The most notable difference between these systems is at the central metal atom. Each M-O bond predominately results from interaction of the d orbital on the metal with the s and p orbitals on the oxygen to give σ- and π-bonding, respectively. However, the f block systems show f orbital mixing in the M-O bonds, and this f character can be seen in the M-O bonding NLMOs shown in Figure 2 for $U(OC_6H_5)_4$, which has more lobes at the U centre, compared with Ti. Otherwise, there is no discernible variation from visual inspection of the NLMOs. This result, together with the structural similarities evident from Table 1, means that the systems are sufficiently analogous to probe and compare M-O bonding.

The NLMOs can be decomposed to reveal the contributions from the metal atom (%M), and the results of this analysis, using %M as the sum of the 3 bonding-type orbitals (σ + 2π), is shown as a function of *r*(M-O) in Figure 3. Individual M-O bonding NLMOs (σ or π) have less than 15 %M for all systems and thus, are highly polarized bonds. NLMOs with less than 5 %M character are classified as oxygen lone pairs. If σ and average π contributions are considered separately, only Ti, U and Ce have π-bonding NLMOs with greater than 5 %M character. Thus, a divide is found in Figure 3 where the Ti, U and Ce systems have greater total %M than Zr, Hf and Th, with the latter systems being dominated by σ-type bonding.

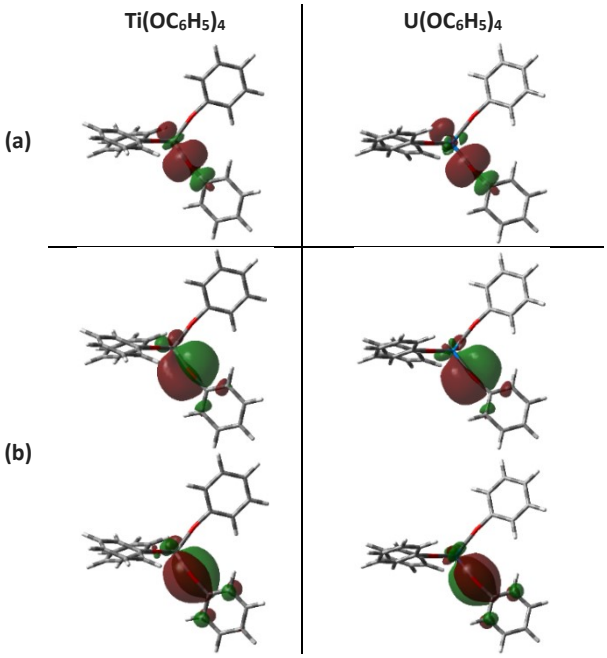

Figure 2: The NLMOs for an M-O bond in $Ti(OC_6H_5)_4$ (left) and $U(OC_6H_5)_4$ (right). The σ-type bonds are shown in (a) and the two π-type bonds are shown in (b). Isosurface value 0.02 au.

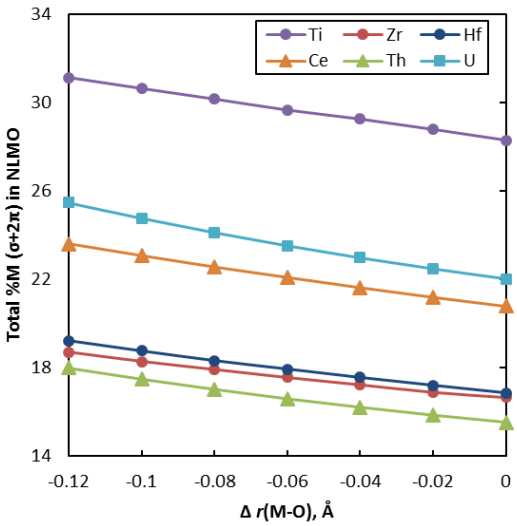

Figure 3: Sum (σ + 2π) of metal contribution, %M, to the M-O bonding NLMOs with changes in *r*(M-O) in $M(OC_6H_5)_4$.

All systems experience increased %M upon shortening of *r*(M-O), with the greatest increase observed for $U(OC_6H_5)_4$, 20-70% larger than for the other systems. In other words, as *r*(M-O) decreases, U most effectively increases metal contribution to the NLMOs. Although the %U contribution increases most steeply in both σ and π bonding, the effect in the latter is the more dramatic, with %U contribution to π bonding increasing by a factor of ca. 2 to 3 times that of the other systems.

The %M contribution to the NLMOs can be decomposed into atomic orbital character, and the results are shown in Figure 4. In each case, the σ and average π orbital composition is shown as a function of orbital character and as a percentage of the total contribution to the NLMO. The results are shown for the optimized system and where *r*(M-O) is shortened by -0.12 Å. The d block systems exhibit predominantly d character in all NLMOs, with minor s contribution to the σ-type bonding. The f block systems also display f orbital character in both σ- and π-type bonding NLMOs. This is most pronounced in π-type bonding where a significant portion of %M is f. The total %M contribution does not correlate with the deformation energy of *r*(M-O) shown in Figure 1 (R^2 = 0.08), however, if only the d character of the M-O bonds is considered a much better correlation is found (R^2 = 0.72). This correlation is found in both the σ (R^2 = 0.68) and π (R^2 = 0.73) orbitals. This suggests a relationship between d orbital involvement in bonding and bond deformability, though not an analogous f relationship. Studies of An-Cp complexes found large f orbital involvement in predominantly Cp-based orbitals which are not believed to contribute significantly to bond strength.[3,31,32]

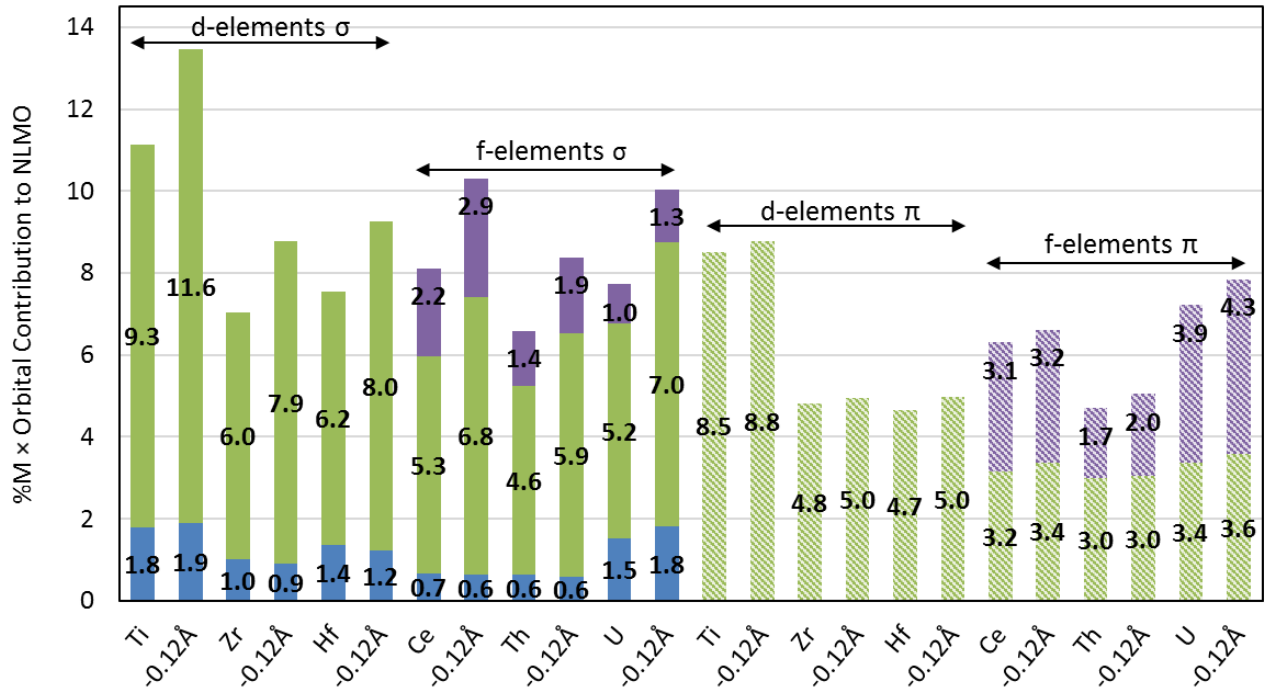

Figure 4: %M contribution to NLMOs for geometry-optimized $M(OC_6H_5)_4$ and at [r(M-O) – 0.12 Å]. %M is decomposed into the atomic orbital type where s, d, and f orbital character are represented by blue, green, and purple colours, respectively. The σ- and π-type NLMOs are shown as solid and striped bars, respectively. The π-type NLMO is an average the two π-type NLMOs. Values ≤ 0.01% are not shown.

The Ce system exhibits the greatest f character (ca. 28 % of the total %M in the optimized system) in σ bonding, and significant f character (ca. 49% of the total %M in the optimized system) in π bonding. The 4f orbitals of the lanthanides are typically considered to be core-like with limited radial extent compared with the 5f orbitals of early actinides; however, covalency in cerium systems has been previously reported, *e.g.* in oxide, halide, and carbene complexes.[33–35] Cerium is unique in the lanthanide series in having a readily accessible tetravalent oxidation state, and our results show similarities in the covalent nature of the $Ce(OC_6H_5)_4$ and $U(OC_6H_5)_4$. Two previous studies[34,35] use QTAIM metrics to report a covalency trend of U > Ce > Th and our results support this result, based on the metal contributions to bonding (Figure 3). This trend can be attributed to the f orbital contribution in π bonding, as the d orbital participation is similar, particularly for Ce and U.

Although it may be tempting to assume that increased %M contribution to a bonding orbital (NLMO) is accompanied by increased overlap between the precursor orbitals, this is not necessarily the case. Consider the simple example of lengthening a homonuclear bond, in which the overlap decreases despite the contribution from each atom remaining constant. Thus, the overlap integrals of the PNHOs were calculated and the results are shown in Figure 5. The trends for overlap in the σ and π bonding separately are shown in Figure SI1 and follow similar trends to those in Figure 5. The f block systems show greater overlap, compared with the transition metals, *i.e.* we see larger overlap integrals where bonding orbitals are composed of s, d and f components, by contrast to the transition metal systems where only s and d orbitals contribute to the covalent bonding.

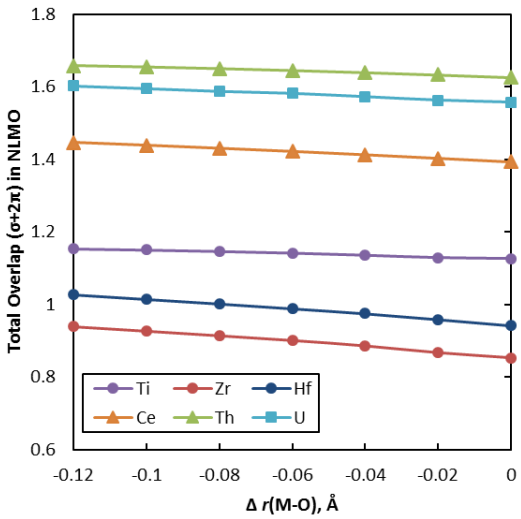

Figure 5: Sum (σ + 2π) of overlap integrals for the M-O bonding NLMOs with changes in r(M-O) in $M(OC_6H_5)_4$.

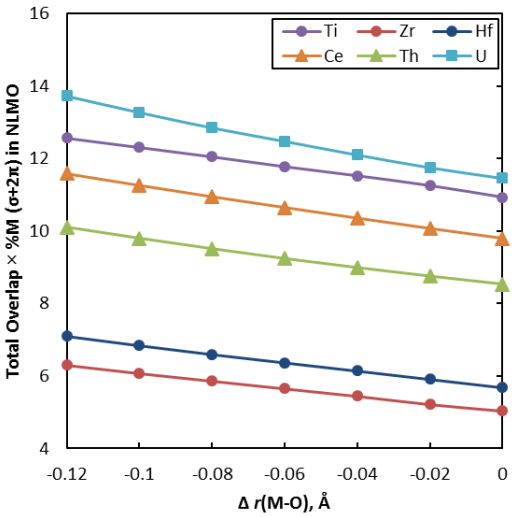

Figure 6: Product of the overlap integrals and %M contribution to the three M-O bonding NLMOs (σ+2π) with changes in *r*(M-O) in $M(OC_6H_5)_4$.

The results for the f block systems are consistent with the trends in radial extension of orbitals within a chemical series, with Th displaying greater overlap than U, and Ce exhibiting less overlap than the actinides, indicative of the greater core-like behaviour of the 4f orbitals. As already noted, the magnitude of overlap does not necessarily infer greater %M contribution. The actinides have greatest overlap, despite Th exhibiting the lowest %M contribution to the NLMOs. Thus, we are reminded that overlap alone does not define bonding and that for Th, although there is significant orbital overlap, the NLMOs are largely dominated by oxygen character. It follows that both properties, overlap and %M contribution, need to be considered when assessing M-O bonding, and we present the product of these in Figure 6. The product is calculated for each of the σ- and π-type orbitals separately, and summed to give the data presented. We propose this metric as a measure of covalency from a localized bonding orbital perspective, revealing a covalency trend of U > Ti > Ce > Th > Hf > Zr; we show further support for this trend in the following section.

Quantum theory of atoms in molecules analysis

Analysis of the topology of the electron density provides another quantitative measure of bonding, that differs from orbital based methods such as NBO. In this section the quantum theory of atoms in molecules is used to further analyse M-O covalency in $M(OC_6H_5)_4$. The metrics employed herein have been used extensively to characterize bonding *in situ* and have been shown to be particularly useful in f element chemistry.[4,31,36–39]

Data for the bond critical point (BCP) metrics (electron density, ρ_{BCP}, its Laplacian $\nabla^2\rho_{BCP}$, and the total energy density H_{BCP}) and integrated QTAIM properties (atomic charge, *q*, and the delocalization index of the M and O atom pair, δ(M,O)) are shown in Table 2 for the optimized $M(OC_6H_5)_4$ systems (and for the systems at *r*(M-O) – 0.12 Å in Table SI2 of the Supplementary Information). The magnitudes of ρ_{BCP} and H_{BCP} are measures of covalency, where values of $\rho_{BCP} > 0.2$ au and $H_{BCP} < 0$ indicate interactions with significant sharing of electrons, or covalent character.[40] Interestingly, there is a strong correlation between the deformation energy of *r*(M-O), presented in Figure 1, and ρ_{BCP} and H_{BCP} for the transition metal systems, such that $R^2 = 1.00$ and $R^2 = 0.91$, respectively (Figure SI2b and SI3b). However, the f block systems do not exhibit any such correlation, such that $R^2 = 0.00$ and $R^2 = 0.01$ for ρ_{BCP} and H_{BCP}, respectively (Figure SI2c and SI3c). We have previously seen very poor correlations of ρ_{BCP} and H_{BCP} with bond energies in systems featuring An–N bonds.[38] Since bond strength and bond covalency are not synonymous, we suggest that the interplay of d and f orbital contributions to bonding plays a significant role in the distinction between the d and f element systems, and contributes to the variation in ρ_{BCP} and deformation energy of *r*(M-O) reported herein. Covalency trends based on ρ_{BCP} or H_{BCP} for the f block systems (U > Ce > Th) agree with the orbital analysis presented above, and with previous studies.[34,35]

Table 2: QTAIM metrics (au) for the optimized $M(OC_6H_5)_4$ systems. Bond critical point metrics for the M-O bond, and integrated properties are presented. QTAIM metrics for *r*(M-O) at -0.12 Å are shown in Table SI2.

M	*r*(M-O), Å	*q*(M)	*q*(O)	ρ_{BCP}	$\nabla^2\rho_{BCP}$	H_{BCP}	δ(M,O)
Ti	1.785	2.33	-1.23	0.146	0.762	-0.047	0.766
Zr	1.937	2.68	-1.29	0.119	0.644	-0.030	0.687
Hf	1.919	2.74	-1.31	0.130	0.757	-0.033	0.666
Ce	2.086	2.49	-1.24	0.112	0.426	-0.037	0.822
Th	2.147	2.84	-1.30	0.107	0.392	-0.034	0.744
U	2.088	2.63	-1.27	0.125	0.482	-0.045	0.856

Atomic charges can give indications of bonding character, with decreased charge (and charge separation) associated with covalency. The QTAIM charges on the metal, *q*(M), show a trend for the transition metals, with covalent behaviour decreasing down the group. For the f block systems, *q*(M) suggests a covalency trend of Ce > U > Th. These trends are consistent with the NBO charges which are shown in Table SI3 of the Supplementary Information.

The Laplacian of ρ_{BCP}, $\nabla^2\rho_{BCP}$, describes the degree of electron density concentration ($\nabla^2\rho_{BCP} < 0$) or depletion ($\nabla^2\rho_{BCP} > 0$) at the BCP. Covalent bonds have build-up of electron density at the BCP, yielding a negative $\nabla^2\rho_{BCP}$, however, the highly polarized nature of the M-O bond herein yields all positive values of $\nabla^2\rho_{BCP}$ and is typical of highly polar bonding. The changes in $\nabla^2\rho_{BCP}$ with *r*(M-O) are shown in Figure 7. Interestingly, the transition metals have the greater values of $\nabla^2\rho_{BCP}$, indicative of greater charge depletion and decreased covalency. Further, the gradient of $\nabla^2\rho_{BCP}$ for the transition metal systems is ca. 2 times that of the f block systems. We have previously observed modest correlations of $\nabla^2\rho_{BCP}$ with bond energies in systems containing An–N bonds.[38]

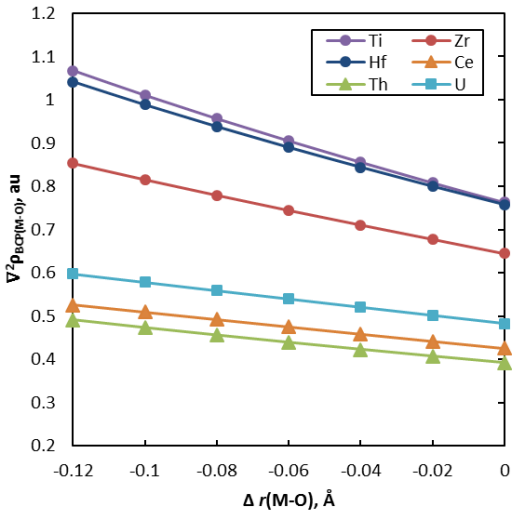

Figure 7: The Laplacian at the BCP, $\nabla^2\rho_{BCP}$, for the $M(OC_6H_5)_4$ systems with changes in *r*(M-O).

To understand the origin and significance of $\nabla^2\rho_{BCP}$ in more detail, we look to the virial theorem (equation 1) and the definition of the total energy density (equation 2). The latter is defined as the sum of the potential (V_{BCP}) and kinetic (G_{BCP}) energy densities and if the potential energy is greater in magnitude, a negative total energy density (H_{BCP}) results.

$$¼\nabla^2\rho_{BCP} = 2G_{BCP} + V_{BCP} \quad (1)$$

$$H_{BCP} = V_{BCP} + G_{BCP} \quad (2)$$

For the bonding interaction investigated herein $|V_{BCP}| > G_{BCP}$ and thus H_{BCP} is negative. However, $|V_{BCP}|$ is not greater than $2G_{BCP}$, hence $\nabla^2\rho_{BCP}$ is positive. The ratio $-(G_{BCP}/V_{BCP})$ provides a measure of partially covalent interactions when between 0.5 and 1, such that as $-(G_{BCP}/V_{BCP})$ approaches 1 the system is more non-covalent.[41] This ratio is shown for the systems considered herein in Table 3, together with changes in the destabilizing kinetic energy density (G_{BCP}).¶ All systems show a decrease in $-(G_{BCP}/V_{BCP})$ ratio with shortening of *r*(M-O), indicating increasing covalent character. The transition metal systems have a greater $-(G_{BCP}/V_{BCP})$ ratio than the f elements, again indicating more covalent character in the f elements. This is a direct result of the greater magnitude of G_{BCP} for the transition metals. Further, the slope of G_{BCP} increases with changes in *r*(M-O) at a rate up to 2 times greater in the transition metals relative to the f block systems.

In the previously presented NLMO-based bonding analysis, it was shown that the f block complexes exhibit greater overlap than the d block systems. This increased overlap manifests itself in the electron density through decrease in kinetic energy of the electrons involved in the associated bonding interaction. The greater magnitude of overlap allows greater delocalization and thus, reduction of kinetic energy density. Hence, as hypothesized for the overlap, we propose that the diversity of the valence region of the f block systems allows greater delocalization of the electron density into valence orbitals and results in attenuation of the destabilizing kinetic energy density.[42] Overall, the $-(G_{BCP}/V_{BCP})$ ratio suggests a covalency trend of U > Ce ≈ Th > Ti > Hf > Zr, with a clear separation between the d and f elements.

Table 3: Kinetic energy density at the M-O BCP, G_{BCP}, and ratio of kinetic to potential energy densities, $-(G_{BCP}/V_{BCP})$ for $M(OC_6H_5)_4$ in the optimized systems and when *r*(M-O) is shortened by 0.12 Å.

Compound	G_{BCP}, au		$-(G_{BCP}/V_{BCP})$	
	Optimized	-0.12 Å	Optimized	-0.12 Å
$Ti(OC_6H_5)_4$	0.237	0.354	0.836	0.802
$Zr(OC_6H_5)_4$	0.191	0.276	0.863	0.814
$Hf(OC_6H_5)_4$	0.196	0.286	0.856	0.811
$Ce(OC_6H_5)_4$	0.143	0.198	0.796	0.749
$Th(OC_6H_5)_4$	0.132	0.184	0.795	0.750
$U(OC_6H_5)_4$	0.165	0.231	0.786	0.738

Essential to the idea of covalent bonding is the exchange of electrons between bonded atoms. The delocalization index is often used as the defining QTAIM metric for covalency, since it provides a measure of the number of electron pairs exchanged in an interaction.[4,9,43–45] It is derived from the expectation value of the exchange operator over two atomic basins and is irrespective of the nature of the interaction. The delocalization indices for M-O bonding, δ(M,O), are shown in Figure 8. It is worth noting that the magnitude of δ(A,B) does not equal the number of electron pairs shared unless they are shared equally and decreases due to unequal sharing or

¶ Formally, the viral theorem holds only for an equilibrium system. However, there are only very small changes to the virial theorem over our range of *r*(M-O). For example, in the U system $|¼\nabla^2\rho_{BCP} - [2G_{BCP} + V_{BCP}]|$ is 4.3×10^{-8} at the optimized geometry, and 3.6×10^{-7} at *r*(M-O) – 0.12 Å.

delocalization elsewhere in the molecule.[45–52] Overall, δ(M,O) predicts a covalency trend of U > Ce > Ti > Th > Zr > Hf.

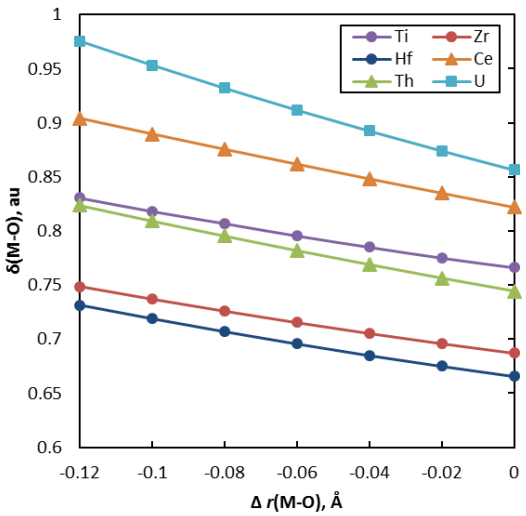

Figure 8: The delocalization index, δ(M,O), for the $M(OC_6H_5)_4$ systems with changes in *r*(M-O).

Comparison of NLMO and QTAIM data

Consistency between the orbital-based NLMO analysis and the electron density-based QTAIM metrics is important for confidence in the conclusions. A summary of the trends predicted by these methods is shown in Table 4. In general, there is remarkably good agreement; the U-O bond exhibits the greatest covalency, followed by Ce and then Th, with the 4d and 5d elements consistently calculated to have the least covalent M-O bonds.

Table 4: Covalency trends for the M-O bond in $M(OC_6H_5)_4$.

Metric	Covalency trend
NLMO: %M × overlap	U > **Ti** > Ce > Th > Hf > Zr
QTAIM: $-(G_{BCP}/V_{BCP})$	U > Ce ≈ Th > **Ti** > Hf > Zr
QTAIM: δ(M,O)	U > Ce > **Ti** > Th > Zr > Hf

The three metrics disagree as to the relative covalency of the Ti system. While it is always found to be the most covalent of the group 4 elements, its position *vs* Ce and Th varies with metric. -(G_{BCP}/V_{BCP}) yields the lowest relative covalency for the Ti system, with a clear divide between the f and d elements. It differs, most relevantly, from the other metrics in being a BCP property. The BCP lies along the bond path, or path of maximum electron density between the nuclear attractors, and is thus most significantly impacted by σ-type bonding interactions. Since the Ti system has the greatest π-type bonding interactions (shown in Figure 4 and Figure SI4) this may play a role in bolstering the NLMO and δ(M,O) metrics for Ti. The $-(G_{BCP}/V_{BCP})$ metric is important in that it characterizes the nature of the electon density at the BCP. The attenuation of kinetic energy density is a key property of covalency, and thus this metric provides an interesting perspective on this trend. The attentuation achieved by the f elements is likely the result of the diversification of the valence region to include s, d, and f orbital contributions, while the d elements are restricted to s and d.

The NLMO metric predicts the Ti–O bond to have the largest relative covalency, compared with the other two metrics. The NLMO metric is the product of the %M contribution, where Ti dominates, and the overlap of the precursory orbitals to the NLMOs, where there is a divide between the d and f elements, with the f elements exhibiting greater overlap. Thus, the factor contributing more significantly to the high NLMO covalency of the Ti system is the %M contribution to the Ti-O bond. Ti has the highest electronegativity of all the metals studied[53] (Pauling electronegativities: Ti 1.54, Zr 1.33, Hf 1.3, Ce 1.12, Th 1.3, U 1.38), and as such its valence orbitals will be closest in energy to the oxygen 2p levels. The denominator in the expression for the orbital mixing coefficients will therefore be smallest for the Ti/O interaction.

δ(M,O) places Ti between the $-(G_{BCP}/V_{BCP})$ and NLMO metrics in relative covalency. It is an integrated property which accounts for the quantity and equality of electron density exchanged between atomic basins, and does not characterize the BCP. Thus, δ(M,O) can capture covalency resulting from π-type intereactions and provides a bridge between the orbital analysis and the BCP-based $-(G_{BCP}/V_{BCP})$ metric.

We quantify the comparison of the trends in Table 4 in Figure SI5, which plots the correlations between the three metrics. There is good correlation between $-(G_{BCP}/V_{BCP})$ and δ(M,O), and (%M × overlap) and δ(M,O), with R^2 = 0.73 and 0.80 respectively, but rather poorer correlation between (%M × overlap) and $-(G_{BCP}/V_{BCP})$ (R^2 = 0.56), for which Ti is clearly an outlier (R^2 rises to 0.91 when Ti is excluded). In general, the consistency between the conclusions from the different metrics does indeed lend confidence in them.

Conclusions

In this study, we bring together molecular orbital and electron density topology-based analysis methods to assess covalency in $M(OC_6H_5)_4$. The M-O bond in $U(OC_6H_5)_4$ is the most covalent, followed by Ce–O and then Th–O, with those in the heavier transition metal compounds being the least so. The relative covalency of the Ti–O bond is found to be metric dependent.

Our conclusion that the f element systems exhibit greater covalent character than structurally similar d element systems agrees with other studies of actinide and transition metal complexes. For example, a recent study of dithiocarbamate complexes, $M(S_2CN^iPr_2)_4$, featuring a similar metal series to our targets – Ti, Zr, Hf, Th, Np – reports covalency trends based on δ(M,S) which agree with those found here.[9] Note, however, that covalency trends for a given bond can be dependent on ligand environment. For example, in the case of M-Cl bonds, X-ray absorption spectroscopy indicates that U exhibits ca. half the covalency of Ti, Zr and Hf in the metallocene dichloride $(C_5Me_5)_2MCl_2$,[7] while U displays larger orbital mixing than Ti, Zr, and Hf in MCl_6^{2-}complexes.[8]

In summary, this study reaffirms that localised orbital and electron topological analyses are useful tools for probing covalency in d and f element–ligand bonding. Decomposition of the Laplacian of the bond critical point electron density into its potential and

kinetic energy density components allows for the assessment of kinetic energy attenuation, a defining feature of covalency, which is closely related to the overlap of bonding orbitals. This reveals a defining difference in transition metal versus f block M-O bonding and provides context to the delocalization index δ(M,O) which is often used to quantify covalency. We present evidence to suggest that the product of the overlap and %M contribution to NLMOs correlates well with QTAIM metrics, and recommend these measures of covalency for analysis of metal-ligand bonding.

Conflicts of interest

There are no conflicts to declare.

Acknowledgements

We thank the EPSRC for funding (Grant: EP/N022122/1). VB, ZW and NK are also grateful to the University of Manchester for computational resources from the Computational Shared Facility and associated support. Data supporting this study are openly available at http://dx.doi.org/10.17632/4fksxrn6c5.1

References

1 M. L. Neidig, D. L. Clark and R. L. Martin, *Coord. Chem. Rev.*, 2013, **257**, 394–406.
2 J. P. Dognon, *Coord. Chem. Rev.*, 2016, **344**, 150–162.
3 N. Kaltsoyannis, *Inorg. Chem.*, 2013, **52**, 3407–3413.
4 A. Kerridge, *Chem. Commun.*, 2017, **53**, 6685–6695.
5 J. R. Walensky, R. L. Martin, J. W. Ziller and W. J. Evans, *Inorg. Chem.*, 2010, **49**, 10007–10012.
6 W. W. Lukens, N. M. Edelstein, N. Magnani, T. W. Hayton, S. Fortier and L. A. Seaman, *J. Am. Chem. Soc.*, 2013, **135**, 10742–10754.
7 S. A. Kozimor, P. Yang, E. R. Batista, K. S. Boland, C. J. Burns, D. L. Clark, S. D. Conradson, R. L. Martin, M. P. Wilkerson and L. E. Wolfsberg, *J. Am. Chem. Soc.*, 2009, **131**, 12125–12136.
8 S. G. Minasian, J. M. Keith, E. R. Batista, K. S. Boland, D. L. Clark, S. D. Conradson, S. A. Kozimor, R. L. Martin, D. E. Schwarz, D. K. Shuh, G. L. Wagner, M. P. Wilkerson, L. E. Wolfsberg and P. Yang, *J. Am. Chem. Soc.*, 2012, **134**, 5586–5597.
9 A. C. Behrle, A. J. Myers, A. Kerridge and J. R. Walensky, *Inorg. Chem.*, 2018, **57**, 10518–10524.
10 E. D. Glendening, J. K. Badenhoop, A. E. Reed, J. A. Carpenter, J E Bohmann, C. M. Morales, C. R. Landis and F. Weinhold, NBO 6.0, Theoretical Chemistry Institute, University of Wisconsin, Madison, 2013.
11 R. F. W. Bader, *Atoms in Molecules: A Quantum Theory*, Oxford University Press, USA, 1990.
12 P. L. Arnold, A. Prescimone, J. H. Farnaby, S. M. Mansell, S. Parsons and N. Kaltsoyannis, *Angew. Chemie Int. Ed.*, 2015, **54**, 6735–6739.
13 J. R. Jeffries, P. Söderlind, H. Cynn, A. Landa, W. J. Evans, S. T. Weir, Y. K. Vohra and G. H. Lander, *Phys. Rev. B*, 2013, **87**, 214104.
14 P. Zhang, B. T. Wang and X. G. Zhao, *Phys. Rev. B - Condens. Matter Mater. Phys.*, 2010, **82**, 1–14.
15 M. J. Frisch, G. W. Trucks, H. B. Schlegel, G. E. Scuseria, M. A. Robb, J. R. Cheeseman, G. Scalmani, V. Barone, B. Mennucci, G. A. Petersson, H. Nakatsuji, M. Caricato, X. Li, H. P. Hratchian, A. F. Izmaylov, J. Bloino, G. Zheng, J. L. Sonnenberg, M. Hada, M. Ehara, K. Toyota, R. Fukuda, J. Hasegawa, M. Ishida, T. Nakajima, Y. Honda, O. Kitao, H. Nakai, T. Vreven, J. A. Montgomery Jr., J. E. Peralta, F. Ogliaro, M. Bearpark, J. J. Heyd, E. Brothers, K. N. Kudin, V. N. Staroverov, R. Kobayashi, J. Normand, K. Raghavachari, A. Rendell, J. C. Burant, S. S. Iyengar, J. Tomasi, M. Cossi, N. Rega, J. M. Millam, M. Klene, J. E. Knox, J. B. Cross, V. Bakken, C. Adamo, J. Jaramillo, R. Gomperts, R. E. Stratmann, O. Yazyev, A. J. Austin, R. Cammi, C. Pomelli, J. W. Ochterski, R. L. Martin, K. Morokuma, V. G. Zakrzewski, G. A. Voth, P. Salvador, J. J. Dannenberg, S. Dapprich, A. D. Daniels, O. Farkas, J. B. Foresman, J. V Ortiz, J. Cioslowski and D. J. Fox, Gaussian 09, Revision D.01, Gaussian, Inc., Wallingford CT, 2009.
16 M. Ernzerhof and G. E. Scuseria, *J. Chem. Phys.*, 1999, **110**, 5029–5036.
17 C. Adamo and V. Barone, *J. Chem. Phys.*, 1999, **110**, 6158–6169.
18 S. Grimme, J. Antony, S. Ehrlich and H. Krieg, *J. Chem. Phys.*, 2010, **132**, 154104.
19 A. D. Becke and E. R. Johnson, *J. Chem. Phys.*, 2005, **123**, 154101.
20 E. R. Johnson and A. D. Becke, *J. Chem. Phys.*, 2005, **123**, 024101.
21 E. R. Johnson and A. D. Becke, *J. Chem. Phys.*, 2006, **124**, 174104.
22 S. Grimme, S. Ehrlich and L. Goerigk, *J. Comput. Chem.*, 2011, **32**, 1456–1465.
23 A. Schäfer, H. Horn and R. Ahlrichs, *J. Chem. Phys.*, 1992, **97**, 2571–2577.
24 A. Schäfer, R. Huber and R. Ahlrichs, *J. Chem. Phys.*, 1994, **100**, 5829–5835.
25 D. Feller, *J. Comput. Chem.*, 1996, **17**, 1571–1586.
26 K. L. Schuchardt, B. T. Didier, T. Elsethagen, L. Sun, V. Gurumoorthi, J. Chase, J. Li and T. L. Windus, *J. Chem. Inf. Model.*, 2007, **47**, 1045–1052.
27 X. Cao, M. Dolg and H. Stoll, *J. Chem. Phys.*, 2003, **118**, 487–496.
28 W. Küchle, M. Dolg, H. Stoll and H. Preuss, *J. Chem. Phys.*, 1994, **100**, 7535–7542.
29 X. Cao and M. Dolg, *J. Mol. Struct. THEOCHEM*, 2004, **673**, 203–209.
30 T. A. Keith, AIMAll, Version 17.11.14, TK Gristmill Software, Overland Park, KS, 2017.
31 M. J. Tassell and N. Kaltsoyannis, *Dalton Trans*, 2010, **39**, 6719–6725.
32 I. Kirker and N. Kaltsoyannis, *Dalton Trans.*, 2011, **40**, 124–131.
33 S. G. Minasian, E. R. Batista, C. H. Booth, D. L. Clark, J. M. Keith, S. A. Kozimor, W. W. Lukens, R. L. Martin, D. K. Shuh, S. C. E. Stieber, T. Tylisczcak and X. Wen, *J. Am. Chem. Soc.*, 2017, **139**, 18052–18064.
34 R. Beekmeyer and A. Kerridge, *Inorganics*, 2015, **3**, 482–499.
35 M. Gregson, E. Lu, F. Tuna, E. J. L. McInnes, C. Hennig, A. C. Scheinost, J. McMaster, W. Lewis, A. J. Blake, A. Kerridge and S. T. Liddle, *Chem. Sci.*, 2016, **7**, 3286–3297.
36 P. L. Arnold, Z. R. Turner, N. Kaltsoyannis, P. Pelekanaki, R. M. Bellabarba and R. P. Tooze, *Chem. - A Eur. J.*, 2010, **16**, 9623–9629.
37 S. M. Mansell, N. Kaltsoyannis and P. L. Arnold, *J. Am. Chem. Soc.*, 2011, **133**, 9036–9051.
38 Q.-R. Huang, J. R. Kingham and N. Kaltsoyannis, *Dalton Trans.*, 2015, **44**, 2554–2566.
39 I. Fryer-Kanssen, J. Austin and A. Kerridge, *Inorg. Chem.*, 2016, **55**, 10034–10042.
40 C. F. Matta and R. J. Boyd, Eds., *The Quantum Theory of Atoms in Molecules: From Solid State to DNA and Drug Design*, Wiley-VCH, Weinheim, Germany, 2007.

41 M. Ziółkowski, S. J. Grabowski and J. Leszczynski, *J. Phys. Chem. A*, 2006, **110**, 6514–6521.
42 M. W. Schmidt, J. Ivanic and K. Ruedenberg, *J. Chem. Phys.*, 2014, **140**, 1–14.
43 V. Vallet, U. Wahlgren and I. Grenthe, *J. Phys. Chem. A*, 2012, **116**, 12373–12380.
44 F. Cortés-Guzmán and R. F. W. Bader, *Coord. Chem. Rev.*, 2005, **249**, 633–662.
45 C. Foroutan-Nejad, S. Shahbazian and R. Marek, *Chem. - A Eur. J.*, 2014, **20**, 10140–10152.
46 X. Fradera, M. A. Austen and R. F. W. Bader, *J. Phys. Chem. A*, 1999, **103**, 304–314.
47 E. Matito, J. Poater, M. Solà, M. Duran and P. Salvador, *J. Phys. Chem. A*, 2005, **109**, 9904–9910.
48 J. Cioslowski and S. T. Mixon, *J. Am. Chem. Soc.*, 1991, **113**, 4142–4145.
49 J. G. Ángyán, E. Rosta and P. R. Surján, *Chem. Phys. Lett.*, 1999, **299**, 1–8.
50 J. Poater, M. Duran, M. Solà and B. Silvi, *Chem. Rev.*, 2005, **105**, 3911–3947.
51 J. Poater, M. Solà, M. Duran and X. Fradera, *Theor. Chem. Accounts Theory, Comput. Model. (Theoretica Chim. Acta)*, 2002, **107**, 362–371.
52 C. Outeiral, M. A. Vincent, Á. Martín Pendás and P. L. A. Popelier, *Chem. Sci.*, 2018, **9**, 5517–5529.
53 M. Winter, WebElements, https://www.webelements.com/, (accessed 9 December 2018).